ChemPhysChem

Articles
doi.org/10.1002/cphc.201901151

Chem
Europ
European C
Societies P

Check for
updates

Segregation of Dispersed Silica Nanoparticles in Microfluidic Water-in-Oil Droplets: A Kinetic Study

Sahana Sheshachala,[a] Maximilian Grösche,[a] Tim Scherr,[b] Yong Hu,[a] Pengchao Sun,[a] Andreas Bartschat,[b] Ralf Mikut,[b] and Christof M. Niemeyer*[a]

Dispersed negatively charged silica nanoparticles segregate inside microfluidic water-in-oil (W/O) droplets that are coated with a positively charged lipid shell. We report a methodology for the quantitative analysis of this self-assembly process. By using real-time fluorescence microscopy and automated analysis of the recorded images, kinetic data are obtained that characterize the electrostatically-driven self-assembly. We demonstrate that the segregation rates can be controlled by the installment of functional moieties on the nanoparticle's surface, such as nucleic acid and protein molecules. We anticipate that our method enables the quantitative and systematic investigation of the segregation of (bio)functionalized nanoparticles in microfluidic droplets. This could lead to complex supramolecular architectures on the inner surface of micrometer-sized hollow spheres, which might be used, for example, as cell containers for applications in the life sciences.

1. Introduction

The self-assembly of materials in microfluidic environments has become a key technology in recent years to explore the fundamentals of supramolecular processes and to develop advanced processing tools for fabrication and integration of materials systems.[1–2] An emerging technology for supramolecular materials assembly is based on the sequence-specific binding properties of nucleic acids.[3] This vibrant field of research, now known as DNA nanotechnology, has become one of the most critical research areas at the interface of chemistry, materials science, biotechnology, and nanotechnology over the last 35 years.[4–10] Despite this impressive progress in the dissemination of methods and concepts from DNA nanotechnology, there is still a great need to integrate nanoscopic DNA structures into larger functional units to enable applications in complex material systems.[10]

In order to bridge the size regime of individual DNA nanostructures with that of micrometer- and millimeter-sized units, the segregation of DNA components in vesicular superstructures was recently reported. For example, Kurokawa et al.

have demonstrated that batch-produced droplets can be stabilized by assembling Y-shaped DNA oligomers on the inner surface of architectures in microfluidic droplets to enable applications at the cationic lipid membrane vesicles. Sequence-specific assembly of the DNA strands leads to the formation of a thin polymeric DNA shell that increases the interfacial tension, elastic modulus, and shear modulus of the droplet surface.[11] Likewise, microfluidically produced water-in-oil (W/O) droplets were recently used to assemble DNA architectures at the inner surface of the droplets taking advantage of DNA hybridization events[12] or electrostatic interactions.[13] Furthermore, the electrostatic assembly of negatively charged silica nanoparticles,[14] gold nanoparticle-modified surfactants, and biomolecule-modified gold nanoparticles[15–16] at the inner interface of W/O droplets has been used to produce mechanically stabilized droplets that can be exploited as containers for biomolecules and cells.

While the examples mentioned above show that the demixing of dispersed colloidal and macromolecular components by electrostatic interaction with complementary polarized interfaces works efficiently and has a high potential for applications, so far, very little has been reported about the kinetics of these segregation processes. Here we report on a methodology for the systematic analysis of particle segregation processes in microfluidically produced W/O droplets using real-time fluorescence measurements (Figure 1). In our method, fluorescently labeled silica nanoparticles are mixed in a dispersed aqueous phase via a flow-focusing junction with a continuous phase of mineral oil and positively charged detergents to produce W/O droplets. Individual droplets are imaged in stop-flow mode with a high-speed camera, and the acquired 2D images are automatically processed using a newly developed MATLAB pipeline to generate fluorescence signal distribution profiles inside the droplets from which quantitative kinetic data can be extracted. By using silica nanoparticles, which have a variable zeta potential and are functionalized with different biomolecular ligands, we demonstrate that the

[a] S. Sheshachala, Dr. M. Grösche, Y. Hu, P. Sun, Prof. Dr. C. M. Niemeyer
Institute for Biological Interfaces (IBG 1)
Karlsruhe Institute of Technology (KIT)
Hermann-von-Helmholtz-Platz 1
76344 Eggenstein-Leopoldshafen, Germany
E-mail: christof.niemeyer@kit.edu
[b] T. Scherr, A. Bartschat, Prof. Dr. R. Mikut
Institute for Automation and Applied Informatics (IAI)
Karlsruhe Institute of Technology (KIT)
Hermann-von-Helmholtz-Platz 1
76344 Eggenstein-Leopoldshafen, Germany

ChemPhysChem

Articles
doi.org/10.1002/cphc.201901151

Chemistry Europe
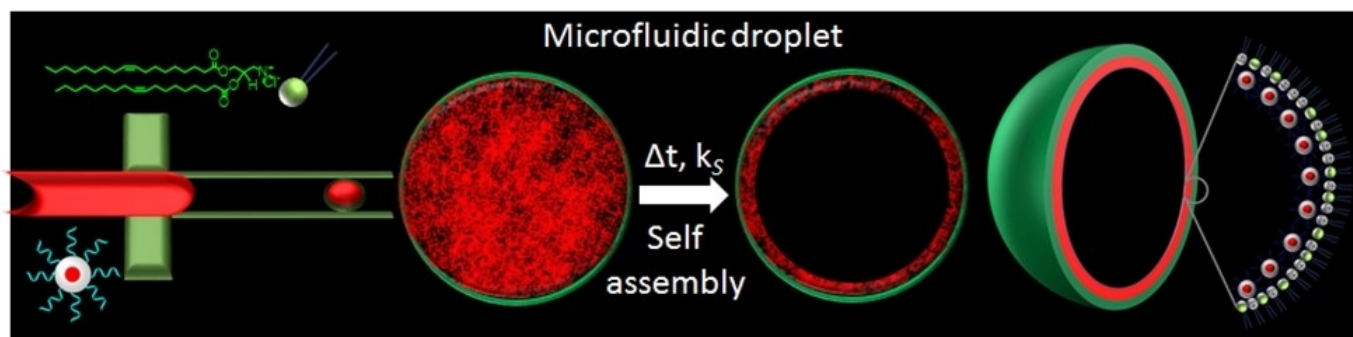European Chemical
Societies Publishing

Figure 1. Schematic representation of the workflow for quantitative assessment of the segregation kinetics of dispersed colloidal silica nanoparticles (SiNP, red) within water-in-oil droplets (green) produced in a microfluidic droplet generating flow-focusing junction structure. The SiNP are injected in the aqueous dispersed phase, whereas mineral oil supplemented with fluorescently labeled positively charged lipid DOTAP (green formula) was used as the continuous phase. Schematic 3D representation and cross-section of the segregated double layer interface of the droplet are shown at the right-hand side.

segregation velocity is mainly influenced by the electrostatic attraction between the particles and the droplet interface. We believe that our work contributes to a better understanding of the self-assembly processes of complex colloidal systems at interfaces and thus to the development of novel self-assembled architectures in microfluidic droplets to enable applications at the interface between materials science, chemistry, and biology.

2. Results and Discussion

2.1. Experimental Setup

To analyze the phase segregation behavior of colloidal SiNP in microfluidic droplets, we used an in-house developed setup that enables generation and monitoring of microfluidic droplets employing real-time fluorescence microscopy imaging. The workflow is shown in Figure 2. An aqueous dispersion of spherically shaped core/shell SiNP (about 90 nm in diameter, as analyzed by TEM, Figure S1 in the Supporting Information) containing a Cy5-fluorescently labeled core was used as a dispersed phase, and mineral oil (MO) supplemented with positively charged 1,2-Dioleoyl-3-trimethylammonium-propane (DOTAP) lipid supplemented with 0.1 mol % of 1,2-dimyristoyl-sn-glycero-3-phosphoethanolamine-N-(lissamine rhodamine B sulfonyl) (Rh-PE) was employed as the continuous phase to generate monodisperse water in oil (W/O) droplets. The two reagent solutions were injected into the inlets of a microfluidic chip made of poly (methyl methacrylate) (PMMA), fabricated by micro-milling, as previously reported.[17] By controlling the flowrates of the aqueous and continuous phase, highly monodispersed W/O droplets of about 180–200 μm diameter were generated with the microfluidic flow-focusing chip. For further analysis, the generated SiNP/DOTAP droplets were then stored in an on-chip storage chamber (OCS).[18]

To analyze the segregation of the dispersed SiNP on the inner surface of the positively charged DOTAP droplets, the microfluidic flow was stopped to enable observation of the generated droplet before it enters the OCS chamber. Typically,

about 60 images of the droplet were captured at a 10-second interval for a 10-minute duration. The obtained images were directly fed into a newly developed MATLAB pipeline (see Section 2.3) specifically designed for automatic detection and quantitative analysis of the fluorescence droplets.

2.2. Segregation of SiNP in DOTAP W/O Droplets

To utilize SiNP colloidal systems for studying the phase segregation process, we synthesized bare silica nanoparticles (**SiNP-1**) using the modified Stoeber method.[19–20] Moreover, three different SiNP [**SiNP-2 (amine)**, **SiNP-3 (BSA)**, and **SiNP-4** (F9), cf. Figure 3] were synthesized by grafting surface functional groups (amine, BSA, and DNA) on bare silica nanoparticles (**SiNP-1**) using a post functionalization method, as previously described.[21] The nanoparticles were fully characterized with respect to their size, surface charge, and functional group density (Figure S1). We found that the various nanoparticles displayed excellent colloidal stability in aqueous solutions, which is an essential prerequisite for the intended segregation studies inside the W/O droplets.

Figure 3 shows representative fluorescence images of the W/O droplets generated with the four different SiNP. The images were taken immediately after production (upper row of images, in Figure 3) or after 10 min of incubation subsequent to production (bottom row). The corresponding fluorescence intensity lines are plotted on top of the droplet images (pink curves, in Figure 3). The diffusion of the SiNP to the inner surface of the droplet is evident by an increase in the fluorescence intensity at the droplet edge (I_E) at the expense of the fluorescence intensity at the center (I_C) of the droplet (Figure 3a).

SiNP-1 (Zeta potential $\zeta = -32$ mV) and DOTAP are oppositely charged[22] and hence diffuse towards the positively charged inner surface of the droplet. As indicated in Figure 3a, this process is clearly evident by comparison of the line profiles obtained from droplets filled with dispersed **SiNP-1** at variable time points. However, notable fluorescence intensity can also
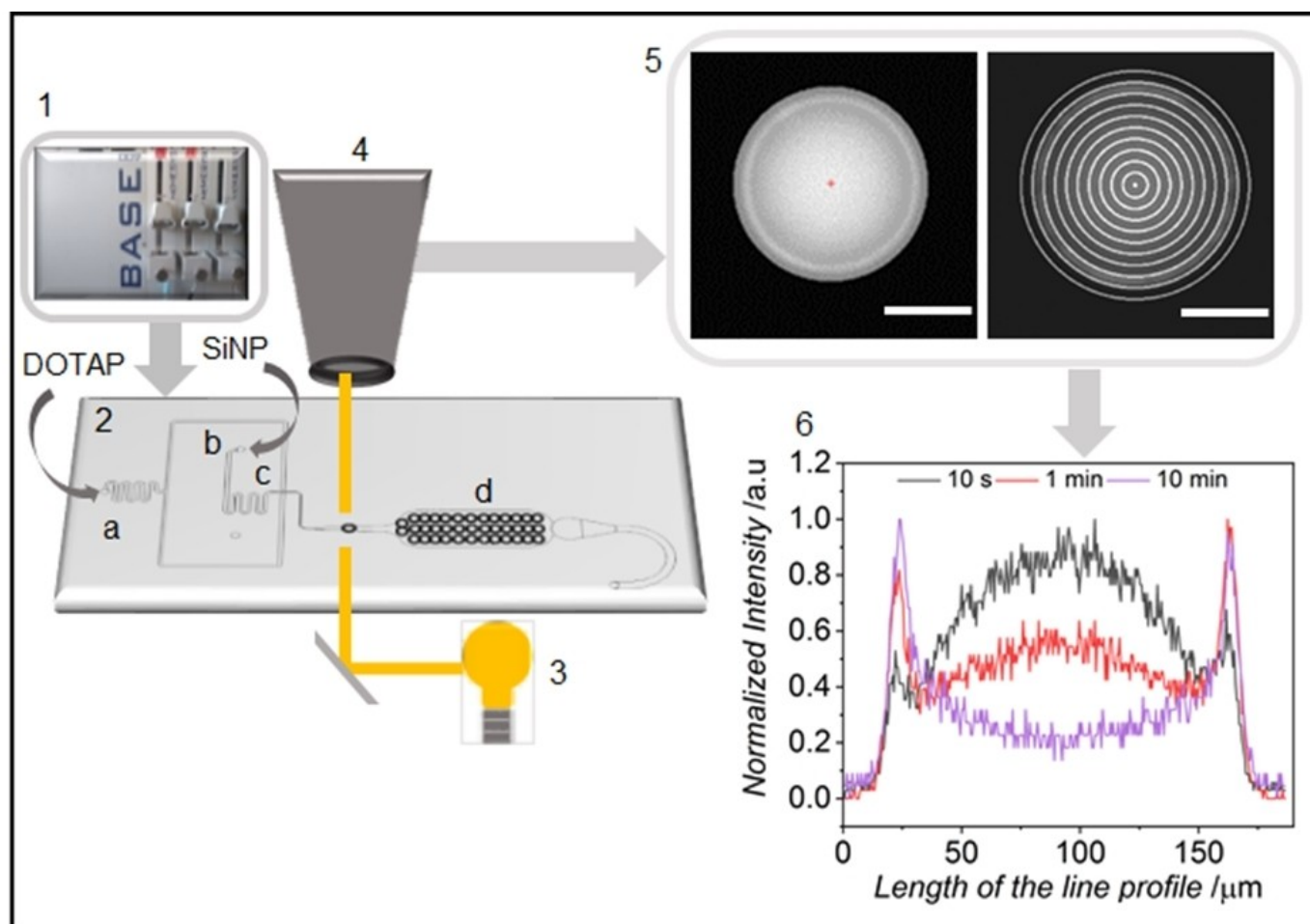
Figure 2. Workflow of the experimental setup for real-time fluorescence measurement of microfluidic water-in-oil (W/O) droplets. (1) Flow controller, (2) Scheme of the microfluidic chip used to produce the W/O droplets, containing inlets for the continuous (a) and dispersed (b) phase, the flow-focusing junction (c), and an OCS chamber (d). The symbols illustrate the arrangement of the light source (3) and the optical path for brightfield and fluorescence imaging (4). Data analysis using a newly developed MATLAB pipeline (5) allows extracting intensity line profiles across the diameter of individual droplets (6). Representative images are shown. Scale bars are 100 μm.

be detected in the droplet's center, suggesting that not all nanoparticles have adhered to the phase boundary of the droplet. This observation was confirmed by extending the measurement time up to 20 min, which did not lead to significant changes in the line profile (data not shown). In contrast to **SiNP-1**, a uniform fluorescence intensity throughout the entire droplet was observed for **SiNP-2 (amine)** ($\zeta = +22$ mV) and **SiNP-3 (BSA)** ($\zeta = -28$ mV), with no indication of segregation underneath the DOTAP lipid within the measured time. This fact is clearly indicated by the respective line profiles obtained from the droplets (Figure 3b, c). In the case of **SiNP-2 (amine)**, this diffusion behavior was expected since particles and membrane are both positively charged; thus, electrostatic repulsion should prevent the particles from adhesion on the membrane. On the other hand, the behavior of **SiNP-3 (BSA)** was somewhat unexpected since the particles have a net negative surface charge ($\zeta = -28$ mV). The isoelectric point of BSA is 4.5–5. While the protein, therefore, has an overall negative charge at pH 6.5, there are also positively charged

domains on the surface, and this might be the reason why no strong electrostatic attraction occurs between **SiNP-3 (BSA)** and the positively charged lipid membrane of the W/O droplets. Furthermore, negligible electrostatic attraction between BSA and DOTAP has previously been observed at measured pH 6.5.[23] We, therefore, conclude that the physisorbed BSA molecules on the particle's surface effectively screen the negative charge of **SiNP-1**,[24] thereby resulting in a weak interaction between **SiNP-3 (BSA)** and the DOTAP shell.

In the case of the DNA oligonucleotide-modified **SiNP-4**, we observed that the fluorescence intensity is rapidly concentrated at the droplet boundary, leaving behind only negligible amounts of the fluorescent particles in the inner part of the droplet volume (Figure 3d, see also Figure S2). This observation suggests a strong electrostatic interaction between the negatively charged **SiNP-4** and the positively charged DOTAP shell, which is in agreement with earlier studies on the electrostatic formation of similar assemblies that employ DNA molecules.[11–13]
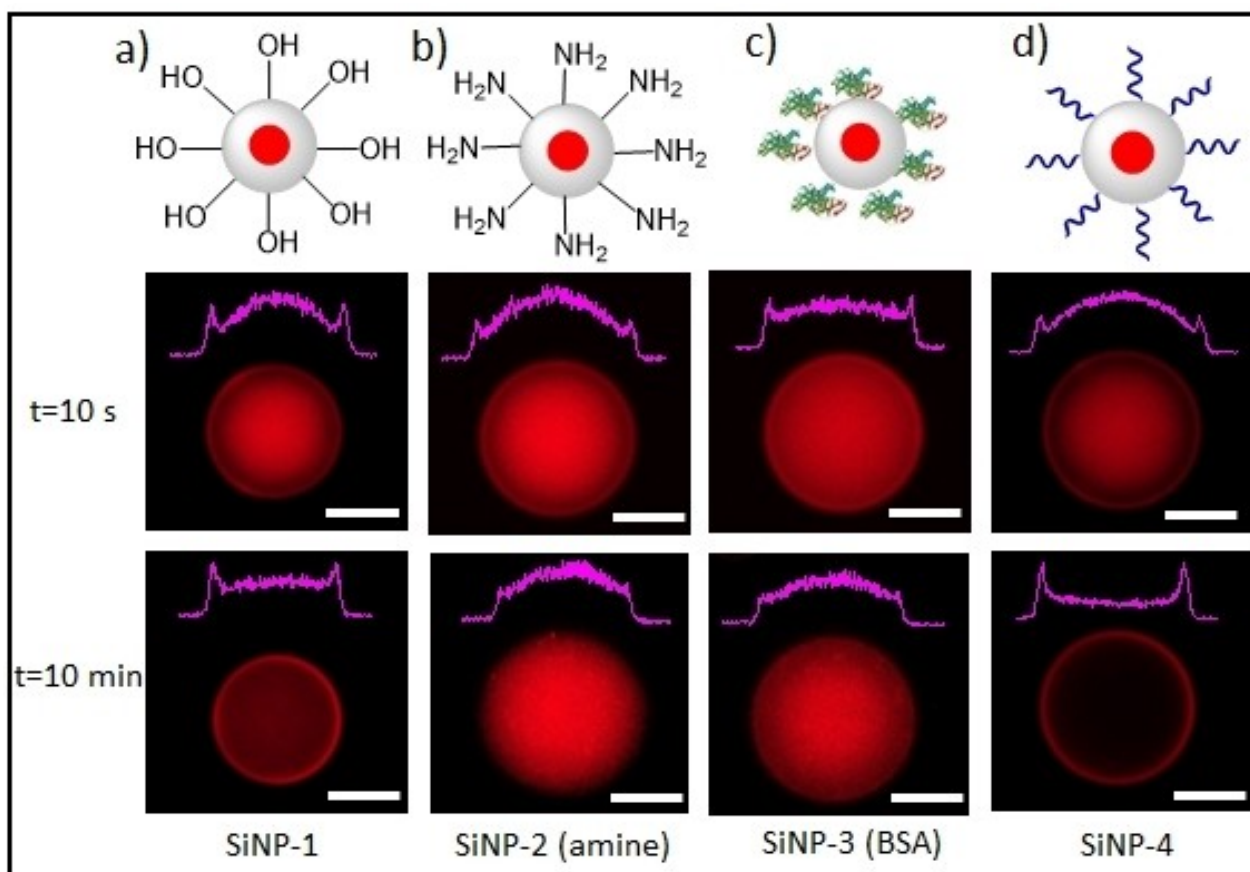
ChemPhysChem

Articles
doi.org/10.1002/cphc.201901151

Chemistry Europe
European Chemical
Societies Publishing

Figure 3. Schematic illustration of four different SiNP bearing variable functional groups and ligands on their surface: (a) bare **SiNP-1**, (b) amine-functionalized **SiNP-2**, (c) BSA-coated **SiNP-3**, and (d) DNA-functionalized **SiNP-4**. The representative fluorescent micrographs below were taken 10 s (top row) or 10 min (bottom row) after droplet generation. The corresponding fluorescence intensity profiles are shown in pink. Scale bar represents 100 μm.

2.3. Image Analysis Pipeline for Quantitative Analysis of Segregation Kinetics

Although all SiNP [except **SiNP-2 (amine)**] have negative zeta potential values (Table 1), we observed that their ability to self-assemble underneath the lipid layer varies from one to another

Table 1. Zeta potential values and kinetic parameters obtained for various SiNP.

Functional group	SiNP	Zeta potential [mV]	$T_{1/2}$ [min]	Slope at $T_{1/2} = k_S$ [min^{-1}]
none	SiNP-1	-31.2 ± 4.5	0.36 ± 0.02	1.08 ± 0.19
amine	SiNP-2	$+22.1 \pm 4.2$	N.A	N.A
BSA	SiNP-3	-28.5 ± 3.8	N.A	N.A
DNA (6-mer)	SiNP-4$_6$	-34.8 ± 1.5	2.27 ± 0.05	0.12 ± 0.01
DNA (22-mer)	SiNP-4$_{22}$	-38.1 ± 2.6	1.02 ± 0.02	0.21 ± 0.01
DNA (40-mer)	SiNP-4$_{40}$	-41.6 ± 2.8	0.51 ± 0.02	0.37 ± 0.02
DNA (22-mer)	MSN-DNA	-36.7 ± 3.6	1.80 ± 0.05	0.16 ± 0.01
F9-STV	SiNP-4(cF9@F9-STV)	-35.8 ± 2.5	1.14 ± 0.13	0.23 ± 0.01

when used at the same concentration. This suggests that not only the electrostatic forces but also other properties of the particles do influence the self-assembly of the SiNP/DOTAP layered architecture. To further elaborate on this phenomenon, we developed a MATLAB-based analysis pipeline that allows the automated extraction of quantitative kinetic data from the recorded microscopy images of the droplets, i.e., the fluorescence intensity at the droplet edges relative to the intensity in the droplet's center is determined over time (I_E, and I_C, respectively, see Figure 3a).

Figure 4 shows the main steps for the evaluation of a single droplet. After an Otsu-based droplet detection and segmentation,[25] the droplet is divided into concentric circles of 3-pixel thickness. The mean and the standard deviation of the intensity within each concentric circle are calculated to get radial intensity profiles, which are interpolated using cubic P-splines.[26] The edge intensity I_E is obtained as the interpolated intensity value of the outer local maximum, whereas the center intensity I_C is the P-spline value at zero distance. In the last step, the asymptotic model $f(t) = a - b \cdot e^{(-ct)}$ with the parameters a, b, and c is fitted to the normalized intensity ratios I_E/I_C of different times (for further details, see Figure S3). The "$T_{1/2}$"-time at which half of the material in the liquid phase is deposited at the

ChemPhysChem

Articles
doi.org/10.1002/cphc.201901151

Chemistry
Europe
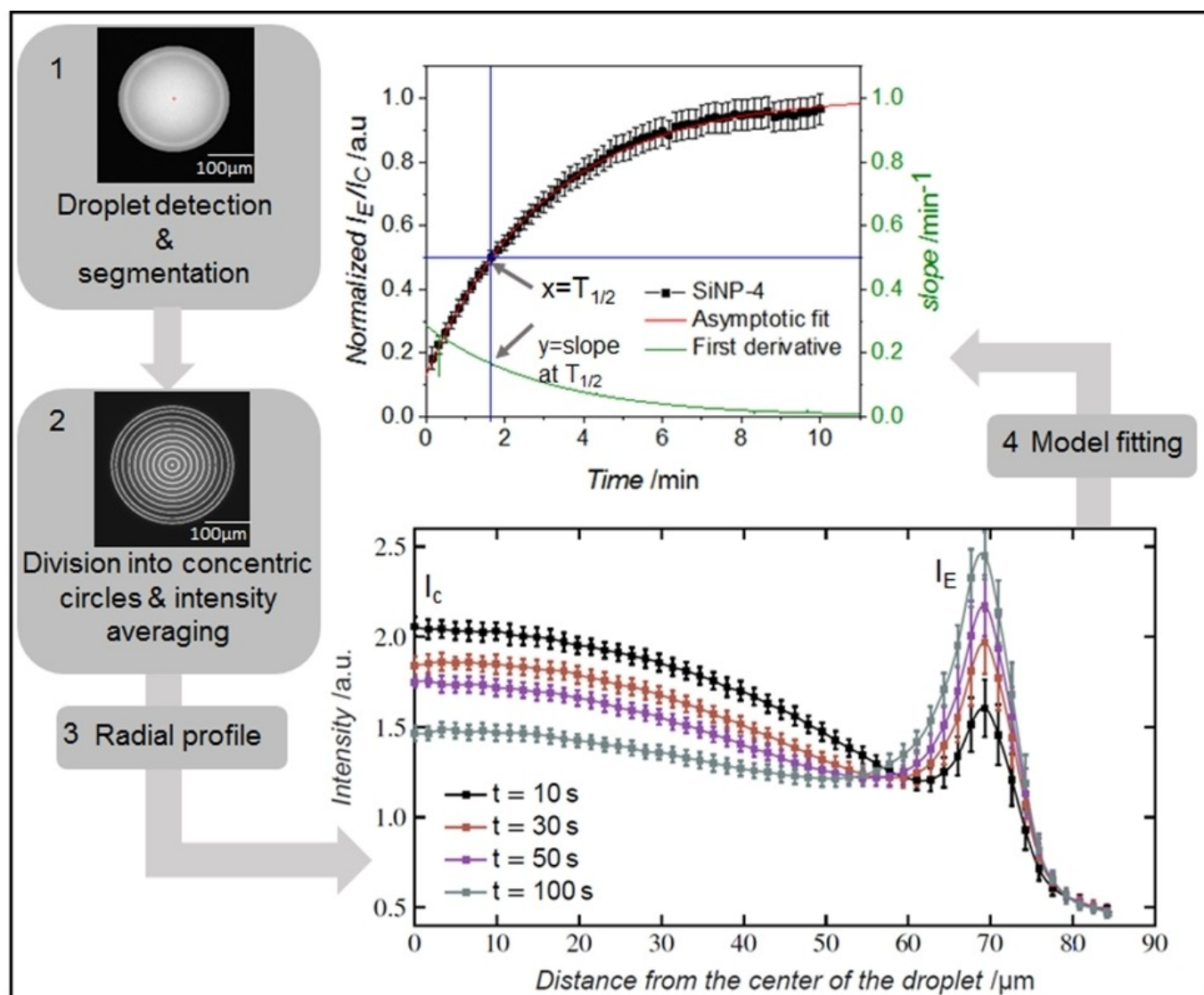European Chemical
Societies Publishing

Figure 4. Graphical representation of the individual analysis steps conducted by the MATLAB pipeline for determining fluorescence intensity profiles of a single droplet. After detection and segmentation (1), a droplet is divided into concentric circles (2, shown is only each fifth circle). The resulting radial intensity profiles are interpolated, and I_C and I_E are calculated (3). The errors of the radial intensities result from the intensity variations within a concentric circle (standard deviation of the N pixels of a concentric circle) and are propagated to the normalized intensity ratios (see Figure S3). The last step (4) includes the fitting of an asymptotic model and the calculation of $T_{1/2}$ and the slope of the curve at $t = T_{1/2}$ (k_S).

interface (blue lines, in Figure 4) is calculated using the fit parameters. Furthermore, the slope of the curve at $t = T_{1/2}$ is calculated using the first derivative of the asymptotic model to yield the kinetic constant k_s, which represents the rate at which SiNP diffuse towards the inner boundary of the droplet.

Each individual droplet image of an experiment was processed with this pipeline. The resulting $T_{1/2}$ times and the corresponding slopes k_S of an experiment were then averaged to quantitatively map the segregation kinetics of various SiNP inside the DOTAP droplets. The reliability of the automated image processing was confirmed by comparison with fluorescence intensity profiles generated manually by using the software provided by the microscope manufacturer (Figure S4).

2.4. Quantitative Analysis of the Segregation Kinetics of SiNP/DOTAP Droplets

Using the MATLAB pipeline to analyze the data obtained from the various particles **SiNP-1-4** (Figure 3) showed that no meaningful results were generated for particles that did not accumulate under the DOTAP shell [**SiNP-2(amine)**, **SiNP-3(BSA)**]. As expected, the I_E/I_C ratio of these particles remained unchanged throughout the measurement time due to their uniform distribution in the droplet. In contrast, MATLAB analysis of the segregation of unmodified **SiNP-1** showed a fast increase in the I_E/I_C ratio and reached a constant regime rapidly, resulting in lower $T_{1/2}$ (0.36 min) and high slope k_S (1.08 min^{-1}) values than other SiNP (Table 1). However, as indicated by the line

profiles, a significant percentage of remaining fluorescence intensity was also detected inside the droplet volume (Figure 3a). This observation suggests that **SiNP-1** rapidly saturated the inner surface of the droplet, thereby effectively shielding the positively charged lipid layer and preventing complete segregation. This also explains the observation that the I_E/I_C ratio rapidly reached a constant regime (Figure S5a).

The DNA coated particles **SiNP-4**, which contained about 80 copies of a 22 mer oligonucleotide on their surface, showed a very sharp segregation (Figure 3d). Thus, we wanted to use the same type of particles to test the precision of our analytical method. To this end, we synthesized a small series of SiNP that contained oligonucleotides of different lengths (6, 22, or 40 mer), resulting in particles denoted as **SiNP-4$_6$**, **SiNP-4$_{22}$**, or **SiNP-4$_{40}$**, respectively. As indicated by experimental data, the amount of oligonucleotides grafted on the surface of **SiNP-4$_6$** to **SiNP-4$_{40}$** was almost identical, whereas their hydrodynamic radii and zeta potential increased with the increasing length of the oligonucleotides (Figure S1). Analysis of their segregation kinetics showed an asymptotic behavior for all the three different particles (Figure S5). The obtained data of $T_{1/2}$ and segregation kinetic constant k_S are graphically represented as box plots in Figure 5. It is immediately evident that segregation velocity increases with oligonucleotide length and, thus, the zeta potential of the individual particles (Table 1).

While it seems reasonable that the higher negative surface potential is the primary driver of the assembly process, it should also be considered that longer oligonucleotides, due to their higher flexibility, can adapt more effectively to a lipid monolayer than shorter DNA molecules.[27] Hence, these results suggest that the increased negative charge and flexibility of longer DNA strands influence the time scales of electrostatic interaction with the DOTAP lipid and also the segregation kinetics inside the droplet.

To further demonstrate the utility of our method we also investigated the influence of SiNP concentration on the segregation kinetics and the thickness of the resulting boundary layer of the droplet (Figure S6). To this end, the concentration of **SiNP-4$_{22}$** was varied from 4 mg/mL to 0.4 mg/mL, and the kinetics, as well as the layer thickness, were determined. Similar $T_{1/2}$ and k_s values indicated that the particle concentration does not significantly affect the initial rate of segregation. However, as expected, the thickness of the resulting SiNP/DOTAP shell varied from about 2.9 to 0.8 μm for **SiNP-4$_{22}$** concentrations of 4 mg/mL to 0.4 mg/mL, respectively. Given the size of a single SiNP of about 90 nm, these data suggest that the NPs assemble into multilayers underneath the DOTAP shell.

We also investigated the influence of ion strength of the solvent by using phosphate-buffered saline (PBS) buffer containing 100 mM NaCl. Since the previously used nanoparticles were unstable under these conditions, we synthesized SiNP of similar size by a reversed micellar method, which were stabilized by polyethylenglycol (PEG) groups, as previously described.[36] The resulting **PEG-SiNP-4$_{22}$** contained similar amounts of oligonucleotides grafted on their surface and had a similar zeta potential as the regular **SiNP-4$_{22}$** used before (Figure S7). Comparision of segregation kinetics indicated that shell formation occurs in PBS ($T_{1/2}=1.6$ min, $k_S=0.14$ min^{-1}), however, much slower than in water ($T_{1/2}=0.9$ min, $k_S=0.19$ min^{-1}). These results are consistent with the difference in zeta potential of **PEG-SiNP-4$_{22}$** in PBS or water (-21 mV as compared to -38.5 mV, respectively), thereby indicating that ions in the buffer can affect or even shield the charge on the droplet's inner interface and/or on the negatively charged particles (Figures S7, S8).

To further elaborate on the segregation kinetics, we used the DNA-directed immobilization of a covalent conjugate comprised of the protein streptavidin and a 22-mer oligonucleotide complementary to the DNA grafted on **SiNP-4$_{22}$**. The resulting particles denoted as **SiNP-4(cF9@F9-STV)** showed similar segregation as observed for the DNA-modified SiNP
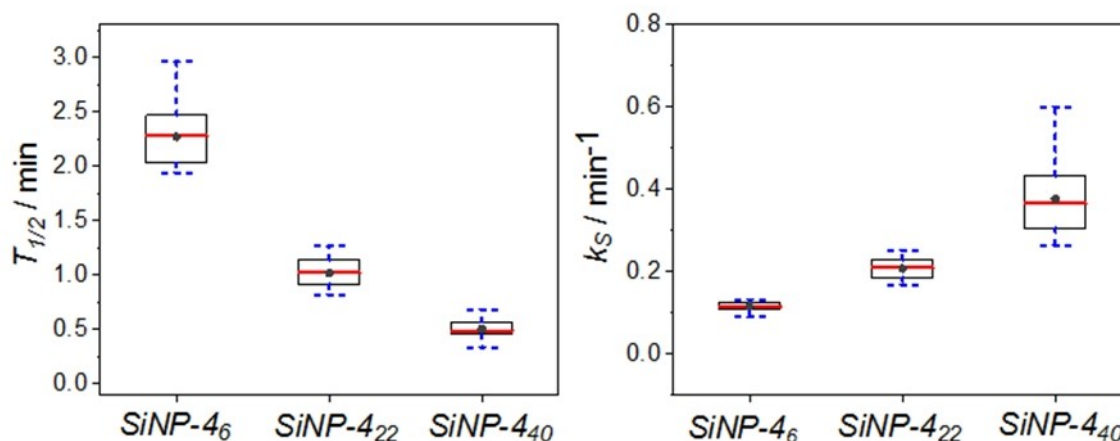

Figure 5. Box plots of $T_{1/2}$ and kinetic constant k_S determined for **SiNP-4** modified with oligonucleotides of different lengths (6,22,40 mer). Median, mean, interquartile range (25−75%), and 2nd and 98th percentile range are indicated in red lines, grey points, black boxes, and blue dash lines, respectively.

(Table 1, see also Figure S9). However, quantitative data analysis revealed that no significant change in the kinetics (Table 1) resulted from the hybridized protein conjugate, as indicated by the fact that $T_{1/2}$ and k_S are similar to **SiNP-4$_{22}$**. This suggests that the low amounts of approximately 35 conjugate molecules anchored on the particles are insufficient to significantly affect the particle's segregation kinetics. Indeed, this hypothesis is supported by the almost unchanged ζ value (Figure S1). This result is of great importance for further developments in the segregation-driven assembly of materials because the implementation of DNA-directed immobilization of DNA-protein conjugates[28] opens up countless possibilities. For example, antibodies or other ligands could be spatially organized by means of SiNP at the inner surface of microfluidic droplets, thus leading to micrometer-sized hollow bodies, which could be used as containers for biomolecules or cells.

We also established, as a proof-of-concept, that other types of DNA-modified silica nanoparticles can be analyzed by our method. Specifically, we confirmed that mesoporous silica nanoparticles (MSN) modified with single-stranded DNA oligomers on their surface,[29] here denoted as **MSN-DNA** (Table 1), can as well be employed in the self-assembly process at the inner surface of DOTAP droplets (Figure S10). Since MSN can be used as nanocontainers for targeted delivery of small molecules, these results open up further perspectives for the development of highly functional supramolecular architectures within microfluidic droplets, which could be used, for example, for the cultivation and analysis of cells.

3. Conclusions

We here report a methodology for the quantitative analysis of the segregation of dispersed silica nanoparticles inside microfluidic water-in-oil (W/O) droplets. By using real-time fluorescence microscopy and automated analysis of the recorded images, kinetic data were obtained that characterize the self-assembly of negatively charged nanoparticles underneath the positively charged lipid layer of the W/O droplets. Using this methodology, we could show that the segregation rates can be controlled by manipulation of the nanoparticle's surface properties.

Our results show that this process is mainly driven by electrostatic interaction; however, it is also evident that additional interactions occurring between the lipid layer at the droplet interface and particle-bound surface groups, such as BSA moieties or DNA strands of different lengths, can have an influence on the segregation kinetics. Phase segregation processes of materials inside confined environments has been studied using polymers, nanocomposites, and bio-functional moieties.[12–16,30] However, to the best of our knowledge, no quantitative and systematic study of nanoparticle segregation inside microfluidic droplets has yet been reported. We believe that our method will contribute to the further refinement of this approach in order to enable a variety of applications in the life sciences, such as the fabrication of cell containers for miRNA

detection on the single-cell level[31] or functional cell screenings.[32]

Experimental Section

Materials

Tetraethyl orthosilicate (99%, TEOS, Merck), (3-mercaptopropyl) trimethoxysilane (95%, MPTMS, Merck), N1-(3-trimethoxysilylpropyl) diethylenetriamine) (DETAPTMS, Merck), (3-aminopropyl) triethoxysilane (99%, APTES, Merck) 2,2′-Dithiodipyridine (DTDP, Merck), Ethanol anhydrous (Merck). Bovine Albumin Serum (BSA) (Alfa Aesar), Triethanolamine (TEA, 99%, Merck), 1,2-dioleoyl-3-trimethylammonium-propane (DOTAP chloride salt, Avanti Polar Lipids),1,2-dimyristoyl-sn-glycero-3-phosphoethanolamine-N-(lissamine rhodamine B sulfonyl) (Rh-PE ammonium salt, Avanti Polar Lipids), Mineral oil (Carl Roth), Sulfo-cyanine 5 NHS-ester (Lumiprobe), Dithiothreitol (DTT, VWR chemicals). Ammonium hydroxide (25%, Merck), Sodium Chloride (NaCl, VWR chemicals),Fluorescamine (98%,Merck), Tris(2-carboxyethyl)phosphine hydrochloride solution (TCEP, 0.5 M, Merck). Sodium-dihydrogen phosphate (Roth), Disodium hydrogen phosphate (Merck).

Synthesis of SiNP-1

The Stoeber particles **SiNP-1** were prepared according to an adapted procedure of the Wiesner group.[33] Typically, 2-propanol (54.5 mL) and water (36 mL) were mixed and thoroughly stirred at 70°C for 1 h, followed by addition of TEOS (1 mL), ammonium hydroxide (25%, 6 mL) and APTES–Cy5 conjugate (250 μL, 5 mg/mL in EtOH). APTES–Cy5 was prepared by mixing cyanine 5 NHS-ester with APTES (10 eq.) in anhydrous EtOH for 12 h and used without further purification. After one hour of reaction, a fresh portion of TEOS (0.5 mL) was added and stirred for an additional 60 min. Following, Cy5-SiNP were purified by centrifugation in water five times. The products were resuspended in Milli-Q water to obtain a stock solution with a final concentration of 10 mg/mL. The stock solution was stored in ethanol until further use. Methodologies and results of the quantification of functional groups (i.e. amine groups (**SiNP-2**), BSA (**SiNP-3**), and ssDNA (**SiNP-4**) are indicated in Figure S1.

Synthesis of SiNP-2 (amine)

For the amine group conjugation, **SiNP-1** (1 mL, 5 mg/mL) were dispersed in ethanol: water mixture (9:1), followed by the addition of 50 μL of DETAPTMS solution and stirring for 24 h. The obtained particles were purified with ethanol and water and stored as described above.

Synthesis of SiNP-3 (BSA)

For the attachment of the BSA solution, we followed a slightly modified protocol from Foldbjerg et al.[34] Typically, **SiNP-1** (2 mg/mL) were dispersed in 10 mM NaCl solution containing 20 mg/mL BSA at pH 4 and incubated at 4°C for 24 h. BSA adsorbed particles were purified several times with water to remove loosely bound protein molecules and dispersed to a final concentration of 10 mg/mL.

ChemPhysChem

Articles
doi.org/10.1002/cphc.201901151

Chemistry
Europe
European Chemical
Societies Publishing

Synthesis of SiNP-4

For the covalent attachment of DNA, **SiNP-1** was first modified with MPTMS to install thiol groups on their surface using a previously reported method.[21] In brief, **SiNP-1** were dispersed in ethanol (1 mL, 10 mg/mL), followed by the addition of TEA (5 μL) and MPTMS (80 μL) The mixture was stirred at 60 °C to obtain thiolated particles. These particles (10 mg/mL in ethanol) were mixed with DTDP (50 mg/mL, 500 μL) and stirred overnight at RT to generate pyridine activated particles. After washing with ethanol for five times, the particles were transferred to water and mixed with thiol-modified oligonucleotides (10 nmol) of variable length and sequence (see Table S1). After incubation overnight at RT and purification with water, the resulting **SiNP-4$_6$**, **SiNP-4$_{22}$**, **SiNP-4$_{40}$** were obtained. For the activation of thiolated oligonucleotides (100 μL, 100 μM), they were incubated with DTT (60 μL, 1 M, 37 °C) for two hours. The oligonucleotides were then purified with NAP-5 and NAP-10 column according to a previously described procedure.[29]

Synthesis of PEG-SiNP-4$_{22}$

PEG-SiNP-4$_{22}$ were synthesized using the previously described protocol.[36] The resulting pegylated nanoparticles were stored either in water or PBS buffer for further use.

Synthesis of MSN-DNA

For the synthesis of **MSN-DNA**, MSN grafted with thiol groups were synthesized and modified with thiolated oligonucleotides (22 mer, Table S1) using the previously reported protocol.[29] The resulting **MSN-DNA** were stored in water until further use.

Synthesis of SiNP-cF9@F9-STV

SiNP-cF9 was synthesized using same method as **SiNP-4** (see above). The DNA-streptavidin conjugate **F9-STV** was synthesized according to established protocols.[35] For hybridization, **F9-STV** conjugate (210 μL, 8 μM in PBS buffer) was mixed with **SiNP-cF9** (10 mg/mL, 200 uL) in PBS buffer (pH = 7.4) and allowed to hybridize overnight at room temperature. The resulting **SiNP-cF9@F9-STV** particles were washed with water for three times.

Physiochemical characterization of SiNP

The hydrodynamic size and zeta potential of SiNP were analyzed at room temperature using a Malvern Zetasizer, Nano ZSP, equipped with a standard 633 nm laser. Transmission electron microscopy (TEM, EM910, Carl Zeiss) was used to measure the size of the nanoparticles.

Quantification of functional groups

The quantification of amine (**SiNP-2**) and thiol (**SiNP-4**) groups was achieved by the fluorescamine assay and Ellman's assay, respectively, using the previously described protocol.[36] The conjugated oligonucleotides and BSA were quantified using the supernatant depletion method by measuring the absorbance of the supernatant at 260 nm (for DNA) and 280 nm (for BSA) before and after the conjugation reaction.[29]

Microfluidic generation of SiNP/DOTAP droplet

For generating SiNP/DOTAP water in oil droplets, particles were dispersed in Milli-Q water using a concentration of 4 mg/mL, and DOTAP was dissolved in mineral oil at 4 mM concentration. The flowrates used were 0.1 μL/min and 4.5 μL/min for the dispersed and continuous phase, respectively. To obtain fluorescence images of the droplets, the inlet flow was stopped to halt the droplet before it enters the storage chamber, approximately 5–8 seconds after the droplet was generated in the flow-focusing junction. Fluorescent images were taken every 10 seconds for a total of 10 minutes using a Zeiss Observer microscope. Droplet generation was also monitored via a high-speed camera (Ximea, Germany). The thickness of the SiNP/DOTAP shell was determined from 2D cross-section images of the droplets obtained with a ZEISS LSM 880 confocal fluorescence microscope.

Conflict of Interest

The authors declare no conflict of interest.

[1] H. Song, D. L. Chen, R. F. Ismagilov, *Angew. Chem.* **2001**, *113*, 3443–3453; **2006**, 45, 7336–7356.
[2] S. Sevim, A. Sorrenti, C. Franco, S. Furukawa, S. Pané, A. J. deMello, J. Puigmartí-Luis, *Chem. Soc. Rev.* **2018**, *47*, 3788–3803.
[3] N. C. Seeman, *Nature* **2003**, *421*, 427–431.
[4] D. Yang, M. R. Hartman, T. L. Derrien, S. Hamada, D. An, K. G. Yancey, R. Cheng, M. Ma, D. Luo, *Acc. Chem. Res.* **2014**, *47*, 1902–1911.
[5] M. R. Jones, N. C. Seeman, C. A. Mirkin, *Science* **2015**, *347*, 1260901.
[6] F. Hong, F. Zhang, Y. Liu, H. Yan, *Chem. Rev.* **2017**, *117*, 12584–12640.
[7] Q. Hu, H. Li, L. Wang, H. Gu, C. Fan, *Chem. Rev.* **2019**, *119*, 6459–6506.
[8] M. Madsen, K. V. Gothelf, *Chem. Rev.* **2019**, *119*, 6384–6458.
[9] F. C. Simmel, B. Yurke, H. R. Singh, *Chem. Rev.* **2019**, *119*, 6326–6369.
[10] Y. Hu, C. M. Niemeyer, *Adv. Mater.* **2019**, *31*, e1806294.
[11] C. Kurokawa, K. Fujiwara, M. Morita, I. Kawamata, Y. Kawagishi, A. Sakai, Y. Murayama, S.-i. M. Nomura, S. Murata, M. Takinoue, M. Yanagisawa, *Proc. Natl. Acad. Sci. USA* **2017**, *114*, 7228–7233.
[12] K. Jahnke, M. Weiss, C. Frey, S. Antona, J.-W. Janiesch, I. Platzman, K. Göpfrich, J. P. Spatz, *Adv. Funct. Mater.* **2019**, *29*, 1808647.
[13] Y. Hu, M. Grosche, S. Sheshachala, C. Oelschlaeger, N. Willenbacher, K. S. Rabe, C. M. Niemeyer, *Angew. Chem. Int. Ed.* **2019**, *58*, 17269–17272.
[14] A. Toor, S. Lamb, B. A. Helms, T. P. Russell, *ACS Nano* **2018**, *12*, 2365–2372.
[15] I. Platzman, J.-W. Janiesch, J. P. Spatz, *J. Am. Chem. Soc.* **2013**, *135*, 3339–3342.
[16] M. Weiss, J. P. Frohnmayer, L. T. Benk, B. Haller, J.-W. Janiesch, T. Heitkamp, M. Börsch, R. B. Lira, R. Dimova, R. Lipowsky, E. Bodenschatz, J.-C. Baret, T. Vidakovic-Koch, K. Sundmacher, I. Platzman, J. P. Spatz, *Nat. Mater.* **2017**, *17*, 89.
[17] M. Grosche, A. E. Zoheir, J. Stegmaier, R. Mikut, D. Mager, J. G. Korvink, K. S. Rabe, C. M. Niemeyer, *Small* **2019**, *15*, e1901956.

ChemPhysChem

Articles
doi.org/10.1002/cphc.201901151

Chemistry Europe
European Chemical
Societies Publishing

[18] M. Grösche, J. G. Korvink, K. S. Rabe, C. M. Niemeyer, *Chem. Engin. Technol.* **2019**, *42*, 2028–2034.

[19] W. Stöber, A. Fink, E. Bohn, *J. Colloid Interface Sci.* **1968**, *26*, 62–69.

[20] A. Van Blaaderen, A. Vrij, *Langmuir* **1992**, *8*, 2921–2931.

[21] A. Leidner, S. Weigel, J. Bauer, J. Reiber, A. Angelin, M. Grösche, T. Scharnweber, C. M. Niemeyer, *Adv. Funct. Mater.* **2018**, *28*, 1707572.

[22] A. Luchini, G. Vitiello, *Frontiers Chem.* **2019**, *7*.

[23] G. Xu, C. Hao, L. Zhang, R. Sun, *Sci. Rep.* **2018**, *8*, 407.

[24] F. Catalano, G. Alberto, P. Ivanchenko, G. Dovbeshko, G. Martra, *J. Phys. Chem. C* **2015**, *119*, 26493–26505.

[25] N. Otsu, *IEEE Transact Sys Man Cybernetics* **1979**, *9*, 62–66.

[26] P. H. C. Eilers, B. D. Marx, *Statist. Sci.* **1996**, *11*, 89–121.

[27] S. Even-Chen, Y. Barenholz, *Biochim. Biophys. Acta - Biomembranes* **2000**, *1509*, 176–188.

[28] A.-K. Schneider, C. M. Niemeyer, , *Angew. Chem. Int. Ed.* **2018**, *57*, 16959–16967.

[29] P. Sun, A. Leidner, S. Weigel, P. G. Weidler, S. Heissler, T. Scharnweber, C. M. Niemeyer, *Small* **2019**, *15*, e1900083.

[30] J. Liu, Y. Lan, Z. Yu, C. S. Y. Tan, R. M. Parker, C. Abell, O. A. Scherman, *Acc. Chem. Res.* **2017**, *50*, 208–217.

[31] S. Guo, W. N. Lin, Y. Hu, G. Sun, D.-T. Phan, C.-H. Chen, *Lab Chip* **2018**, *18*, 1914–1920.

[32] A. I. Segaliny, G. Li, L. Kong, C. Ren, X. Chen, J. K. Wang, D. Baltimore, G. Wu, W. Zhao, *Lab Chip* **2018**, *18*, 3733–3749.

[33] H. Ow, D. R. Larson, M. Srivastava, B. A. Baird, W. W. Webb, U. Wiesner, *Nano Lett.* **2005**, *5*, 113–117.

[34] R. Foldbjerg, J. Wang, C. Beer, K. Thorsen, D. S. Sutherland, H. Autrup, *Chem.-Biol. Interact.* **2013**, *204*, 28–38.

[35] R. Wacker, C. M. Niemeyer, *Curr. Protoc. Nucleic Acid Chem.* **2005**, Chapter 12, Unit 12–17.

[36] X. D. Wang, K. S. Rabe, I. Ahmed, C. M. Niemeyer, *Adv. Mater.* **2015**, *27*, 7945–7950.